Thermal Annealing of Graphene Implanted with Mn at Ultra-Low Energies: From Disordered and Contaminated to Nearly Pristine Graphene

Pin-Cheng Lin,[†,#] Renan Villarreal,[*,†,#] Harsh Bana,[†] Zviadi Zarkua,[†] Vince Hendriks,[†] Hung-Chieh Tsai,[‡,¶] Manuel Auge,[§] Felix Junge,[§] Hans Hofsäss,[§] Ezequiel Tosi,[‖] Paolo Lacovig,[‖] Silvano Lizzit,[‖] Wenjuan Zhao,[‖] Giovanni Di Santo,[‖] Luca Petaccia,[‖] Steven De Feyter,[⊥] Stefan De Gendt,[‡,¶] Steven Brems,[‡] and Lino M. C. Pereira[*,†]

†*Quantum Solid State Physics, KU Leuven, 3001 Leuven, Belgium*

‡*imec vzw (Interuniversitair Micro-Electronica Centrum), 3001 Leuven, Belgium*

¶*Department of Chemistry, Division of Molecular Design and Synthesis, KU Leuven, 3001 Leuven, Belgium*

§*II.Institute of Physics, University of Göttingen, 37077 Göttingen, Germany*

‖*Elettra Sincrotrone Trieste, Strada Statale 14 km 163.5, 34149 Trieste, Italy*

⊥*Department of Chemistry, Division of Molecular Imaging and Photonics, KU Leuven, 3001 Leuven, Belgium*

#*P.-C.L. and R.V. contributed equally to this work*

E-mail: renan.villarreal@kuleuven.be; lino.pereira@kuleuven.be

Phone: +3216323101; +3216320176

Abstract

Ultra-low energy (ULE) ion implantation is increasingly being explored as a method to substitutionally dope graphene. However, complex implantation-related effects such as defect creation and surface contamination, and how they can be minimized by thermal annealing, remain poorly understood. Here, we address these open questions taking as model case epitaxial graphene grown on Cu(111), which was subsequently ULE-implanted with Mn at 40 eV, and then studied as a function of annealing temperature in ultra-high vacuum. While significant surface cleaning occurs at annealing temperatures as low as 200 °C, recovery from the implantation-induced disorder requires at least 525 °C. Upon high-temperature annealing, in the 600-700 °C range, the Mn atoms that were incorporated upon implantation as intercalated species (between graphene and the Cu surface) experience diffusion into the Cu layer, creating a subsurface alloy. Annealing at 700 °C restored implanted graphene to a nearly pristine state, with a well-ordered graphene lattice with substitutional Mn atoms and a well-defined Dirac cone. In addition to the insight into the complex physico-chemical effects induced by thermal annealing, our results provide useful guidelines for future experimental studies on graphene that is modified (*e.g.*, substitutionally doped) using ULE ion implantation.

Introduction

Ultra-low energy (ULE) ion implantation has been successfully used to substitutionally dope graphene, namely with N and B,[1–5] P,[6] Ge[7] and Mn.[8] Although ion implantation in this energy regime (tens of eV) is effective in producing substitutional incorporation with minimal disorder, the resulting systems are highly complex, as non-substitutional incorporation of the implanted atoms, defect formation and surface contamination also occurs.[8] Here, we investigate these undesired effects associated with ULE ion implantation as well as how they can be mitigated, in particular using thermal annealing in ultra-high vacuum (UHV).

In addition to giving insight into the physico-chemical processes, this work provides useful guidelines for future experimental studies on ULE-implanted 2D materials, in particular based on widely-used techniques such as photoemission spectroscopies and scanning probe microscopies.

We take Mn-implanted graphene as a model case, building on recent work where the structural and electronic properties of substitutional Mn in graphene grown on Cu(111) were systematically studied.[8] In particular, substitutional Mn atoms were found to be slightly displaced in the out-of-plane direction, toward the Cu surface. Regarding electronic properties, it was shown that the Dirac-like band structure of graphene is preserved despite the dilute substitutional doping with Mn (of the order of 0.04%), making it an ideal platform for investigating phenomena emerging from the interaction between local magnetic moments and Dirac electrons. However, in addition to the desired incorporation of Mn atoms in substitutional sites, other incorporation forms may also result from the ULE implantation process (figure 1). In the energy regime required for the formation of C vacancies and subsequent substitution (figure 1a), that is, when the ion energy is sufficiently large so that the energy transferred to the carbon recoil atom is larger than the threshold displacement energy ($T_{\mathrm{d}} \approx 21$ eV),[9] a significant fraction of the implanted atoms can also be intercalated into the graphene-substrate interface (figure 1b), or even be incorporated into the substrate, forming a subsurface alloy (figure 1c). Apart from the different forms of incorporation of the implanted atoms, other defects can also be formed (*e.g.*, C vacancies), either from the direct ion impact or from ions that are backscattered from the substrate.[10–13]

Surface contamination must also be taken into account (figure 1d). While even for pristine graphene, exposure to air results in significant hydrocarbon contamination within minutes,[14] the disorder induced upon ion implantation (implanted dopants, vacancies, etc.) is likely to result in a higher surface reactivity. Moreover, the transition-metal substrates where graphene is typically grown are prone to oxidation (*e.g.*, Cu(111)[15,16]) and water intercalation (*e.g.*, Pt(111)[17]) upon exposure to air (figure 1e). Although graphene is impermeable

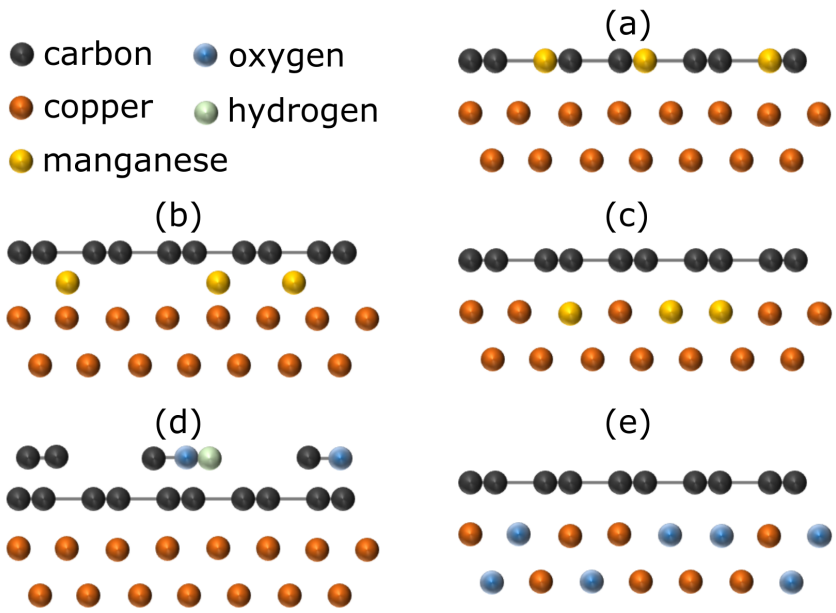

Figure 1: Representation of various forms of incorporation of implanted Mn ions and of surface degradation for graphene on Cu: (a) substitutional Mn, (b) intercalated Mn at the graphene-Cu interface, (c) formation of a subsurface alloy from Cu and implanted Mn, below graphene, (d) adsorbed hydrocarbon contaminants, and (e) Cu oxidation at the graphene-Cu interface.

to any gases and liquids at room temperature (RT),[18] such interfacial contamination is facilitated by the edge (rim) and defects of the graphene grains.[19] As a result of substrate oxidation, the graphene-substrate interaction and thus the properties of graphene (structural and electronic) can be strongly modified.[16,17,20] These effects (non-substitutional incorporation and different forms of disorder and contamination) not only affect the performance of the doped 2D materials, but also make them significantly more challenging to study experimentally. Thermal annealing in UHV is a common mitigation approach, which has been used for decreasing disorder and substrate oxidation and to clean the graphene surface from adsorbates.[15,16,21–23] Here, we study the undesired effects of ULE ion implantation (non-substitutional incorporation and different forms of disorder and contamination) as well as how to mitigate them using thermal annealing in UHV. We focus on Mn implantation with an energy of 40 eV as in reference 8, which is sufficiently high to produce Mn substitution, but still low enough to minimize defect formation. The samples were studied in the as-

implanted state and after subsequent annealing steps in UHV up to 700 °C. Similar studies were performed in non-implanted samples for comparison.

Methods

Our samples consist of epitaxial graphene grown by chemical vapor deposition (CVD) on epitaxial Cu(111) thin films grown on sapphire(0001) substrates; the graphene layer covers the full surface of the Cu/sapphire film.[24] 2 inch polished Czochralski grown sapphire wafers cut along c-plane with <0.1 ° miscut are used to prepare Al_2O_3 template wafers. The as-received wafers are first cleaned in a 3:1 volume ratio of the acid mixture of H_2O_4:H_3PO_4 at 180 °C for 20 min, followed by an ultra pure water rinse for 3 min. Immediately after the cleaning process Cu films are grown. The cleaned sapphire wafers are placed in a Nimbus 310 sputtering setup with a base pressure of 4×10^{-6} mbar. Substrates are placed using a 200 mm Si pocket wafer and sputtering is performed at room temperature for 173 s (21 passes under target) at 6×10^{-3} mbar Ar pressure. The Cu deposition rate is calibrated and corresponds to a rate of about 29 $Å s^{-1}$. The applied power was 3000 W and the throw distance is approximately 50 mm. The graphene growth process has been optimized taking into account oriented monolayer growth and low Raman D peak. The growth conditions are 5000 sccm Ar: 125 sccm H_2: 0.3 sccm CH_4 at a pressure of 750 mbar close to the melting point of Cu. The growth time is 30 min, while ramp-up and down is performed in a mixture of Ar and H_2.

ULE ion implantation was performed by electrostatic deceleration[25,26] of a $^{55}Mn^+$ ion beam from 30 keV to 40 eV, with perpendicular incidence with respect to the sample surface, to a fluence of 1.5×10^{14} ions per cm^2 (fluence rate of 1.7×10^{11} $cm^{-2} \cdot s^{-1}$) measured by integration of the electric current on sample during implantation.[1,3,4,8] The nominal implantation energy (40 eV in the present case) defines the maximum energy of the ions, with an energy distribution that is peaked and truncated at this value, with a tail of the order of

several eV extending to lower energies.[25,26] The samples were annealed *in-situ* with a ramp rate of 1 °C/sec, after reaching the targeting temperature, the temperature was held for 20 minutes in order to make sure of a uniform temperature distribution, afterwards, the samples were cooled down in the UHV (without active cooling). Throughout the annealing process, the vacuum was kept below 5×10^{-8} mbar.

The STM micrographs were obtained in UHV (base pressure $\sim 10^{-10}$ mbar) at room temperature using an Unisoku USM1000, at 78 K using an Omicron LT STM and at 2 K using an Unisoku USM1500. We used electrochemically etched W tips and cut Pt–Ir tips. The tip oxide from the W tips is first removed by flash annealing. Both types of tips were characterized by scanning the Au(111) surface. All topographies were acquired in constant $I_{\text{tun.}}$.

Raman spectra were measured using a confocal Raman microscope (Monovista CRS+, S&I GmbH) equipped with a 532 nm Nd:YAG laser. The laser was directed onto the sample surface through an objective (OLYMPUS, BX43 50×, numerical aperture 0.75), with the maximum laser power remaining below 0.428 mW in order to avoid laser-induced modification. All the measurements were obtained in ambient conditions, at room temperature. The Raman spectra were analyzed after removing the substrate background and the Raman bands were fitted with Lorentzian functions.

LEED measurements were performed in a UHV chamber with background pressure $\sim 4.5 \times 10^{-10}$ mbar using a rear-view LEED (RVL 900) from VG Microtech. The images were recorded using a screen voltage of 1 kV and an electron beam energy of 75 eV (spot size $\approx$ 500 μm at 100 eV).

ARPES measurements were performed at the BaDElPh beamline at Elettra synchrotron in Trieste,[27] with a photon energy of 34 eV. The ARPES spectra were obtained in UHV (base pressure $\sim 5 \times 10^{-11}$ mbar), at 80 K. The presented spectra correspond to a summation of data that were separately acquired using linear p- and s- polarized light. The energy and angular resolution were 10 meV and 0.1 °, respectively.

XPS measurements were performed at the SuperESCA beamline at Elettra synchrotron in Trieste. All the spectra were acquired in UHV (base pressure $\sim 10^{-10}$ mbar) and the samples were placed in the normal emission (NE) configuration, with respect to the hemispherical analyzer. For real-time XPS measurements, the spectra were acquired at a fixed photon energy, considering the time budgets: 650 eV for pristine graphene and 780 eV for Mn-implanted graphene. For high resolution core-level XPS measurements, the photon energies were chosen by optimizing the photoelectric cross section and the surface sensitivity, where the C 1s, O 1s, and Mn 2p core-level spectra were acquired at photon energies of 400 eV, 650 eV, and 780 eV, respectively, with energy resolution always below 150 meV. The binding energy scale has been calibrated with the Fermi level of the metal substrate. The high resolution core-level spectra were fitted with Gauss-Lorentzian sum functions (to approximate a Voigt profile) and a linear background (apart from the Mn 2p core-level data, for which a Shirley background was used). More information about the experimental parameters and their justification is provided in section *Additional XPS details and results* in supporting information.

In order to minimize sample degradation (water intercalation[17,19] and substrate oxidation[16]), the exposure to ambient was kept to a minimum, by storing the samples in a vacuum desiccator (base pressure $\approx 10^{-2}$ mbar). For transportation between different laboratories (between growth, implantation and multiple characterization steps), the samples were sealed in plastic bags at low vacuum (800 mbar), which significantly slows down the process of substrate oxidation during the transportation times (of the order of one day). The samples were only exposed to the atmosphere when they were being manipulated (mounted/dismounted) between different setups, with a typical exposure time of the order of a few minutes per manipulation. All the measurements that are sensitive to surface contamination (XPS, STM, ARPES and LEED), that is, with the exception of Raman spectroscopy, were performed in UHV, and the measurements associated with a given annealing step were performed immediately after annealing in UHV, without breaking vacuum. Raman spectroscopy was performed

in ambient conditions.

Results and discussion

The as-grown graphene on Cu(111) exhibits two main types of defects which are intrinsically at the interface of graphene and the copper substrate, as shown in figure 2a,d. The point-like depressions (some of them indicated by the white arrows) have been related to contaminants as CO[28–30] and O;[31] we will refer to them hereafter as Cu-defects. The nanometer scale patch indicated by the orange arrow is associated with Cu-oxide which can vary from one sample to another and it is in the range of a few percent coverage of the surface.[24] In the as-implanted state, one main additional type of defect appears which is characterized by a nanometer scale circular patch where the atomic lattice of graphene is more easily resolved (some of them indicated by red arrows in figure 2b). Additionally, protruding objects are observed which can be ascribed to adspecies such as residual hydrocarbons, OH groups, displaced C and Cu, and possibly Mn (see figures 2f,g). The as-implanted state often did not allow for a stable tunneling junction (and thus scanning) likely due to contaminants which are unstable on the surface (*e.g.*, hydrocarbons as characterized below via XPS) and may be displaced by the STM tip during the scan. Stable tip topographies as shown in figure 2b could only be acquired after scanning for a couple of times the same area, indicating that the STM tip sweeps the surface from contaminants during the scanning process.[32] We also note that the defect structure corresponding to substitutional Mn, which is characterized by its triangular symmetry,[8] can be found in the as-implanted state (as indicated by the green arrow in figure 2b and crop in figure 2e). Substitutional Mn defects are however more easily resolved after thermal annealing in UHV (figure 2c) as the amount of surface contaminants and other defects are reduced, as discussed in more detail in the following sections. Carbon single vacancies are formed during the implantation process and they are mostly occupied by single Mn atoms. Carbon vacancies can be distinguished from substitutional Mn as

they do not exhibit increased local density of states on the nearest carbon neighbors as the substitutional Mn does.[8] We also note that the moiré superstructure in figure 2a appears to have a different wavelength compared to the one in figure 2c (varying between approximately 4.5 nm and 2.5 nm). Such differences can be explained by small variations (by a few degrees around a typical value of approximately 3 degrees) in the angular mismatch between the graphene and the Cu(111) surfaces in different grains (different regions of the sample).[8]

Surface Cleaning

Table 1: Photoionization Cross-Sections of the C 1s and O 1s Core Levels[33] Corresponding to Photon Energies of 650 eV and 780 eV, Used for the Real-Time XPS Measurements.

photon energy (eV)	C 1s peak	O 1s peak
650	0.1362	0.3383
780	0.0834	0.2176

The effect of thermal annealing in UHV on the surface contamination was characterized using real-time XPS measurements on both Mn-implanted (figure 3) and pristine graphene (figure S1 in supporting information). For Mn-implanted graphene (figure 3), after the thermal annealing in UHV at 200 °C, one of the O components (with binding energy BE $\approx$ 530.5 eV) was strongly reduced, compared to as-implanted state, while no change was observed for the C peak. Detailed peak assignments are discussed below with the help of high-resolution XPS measurements. Then, after annealing in UHV at 425 °C for 20 minutes (figure 3), the integrated peak area of C 1s and O 1s peaks were both reduced by a small percentage: compared to the initial state before annealing (integrated peak area measured at RT), C decreased by 5.5% and O decreased by 8.7% for Mn-implanted graphene; for pristine graphene (figure S1 in supporting information), C decreased by 1.9% and O by 6.3%. In terms of peak position, especially in the spectra of Mn-implanted graphene (figure 3(b, c)), both the C 1s and the O 1s peaks show core-level shifts towards higher BE, implying some changes in the chemical states of the surface. These changes are analyzed in more detail below, using

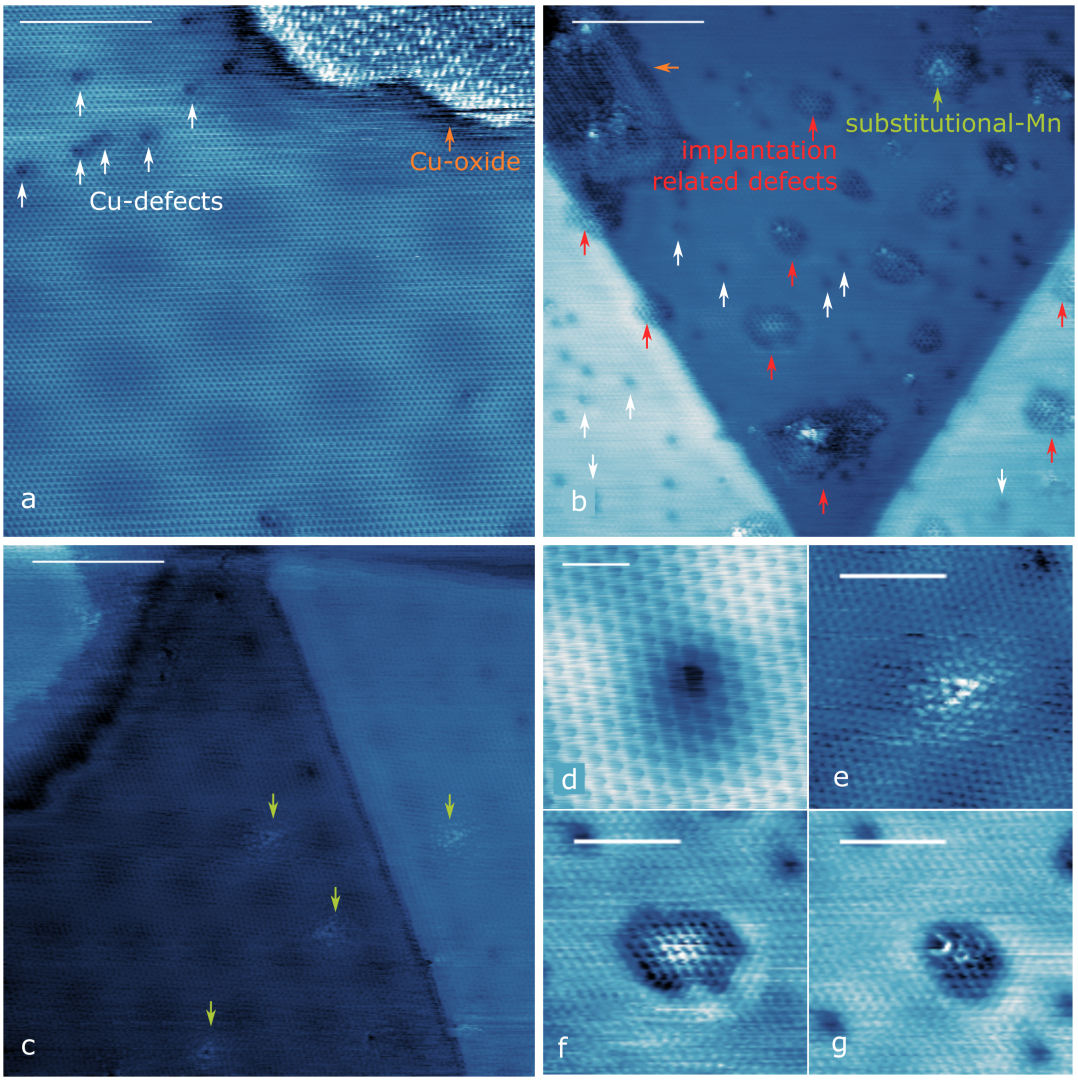

Figure 2: STM topographies of graphene on Cu(111): (a) As-grown (scale bar: 5 nm, V_{sample} = - 300 mV, $I_{\text{tun.}}$ = 100 pA); (b) as-implanted with Mn (scale bar: 5 nm, V_{sample} = 700 mV, $I_{\text{tun.}}$ = 50 pA, scale bar: 5 nm); (c) after 425 °C annealing in UHV (scale bar: 5 nm, V_{sample} = 200 mV, $I_{\text{tun.}}$ = 100 pA); (d) Cu-defect (scale bar: 500 pm, V_{sample} = - 100 mV, $I_{\text{tun.}}$ = 1 nA); (e) crop of (c) on the substitutional Mn (scale bar: 2 nm); (f,g) crop of (b) on the detail on implantation defects (scale bar: 2 nm). White arrows point to intrinsic Cu-defects, orange arrows to intrinsic Cu-oxide, red arrows to implantation related defects, and green arrows to substitutional Mn.

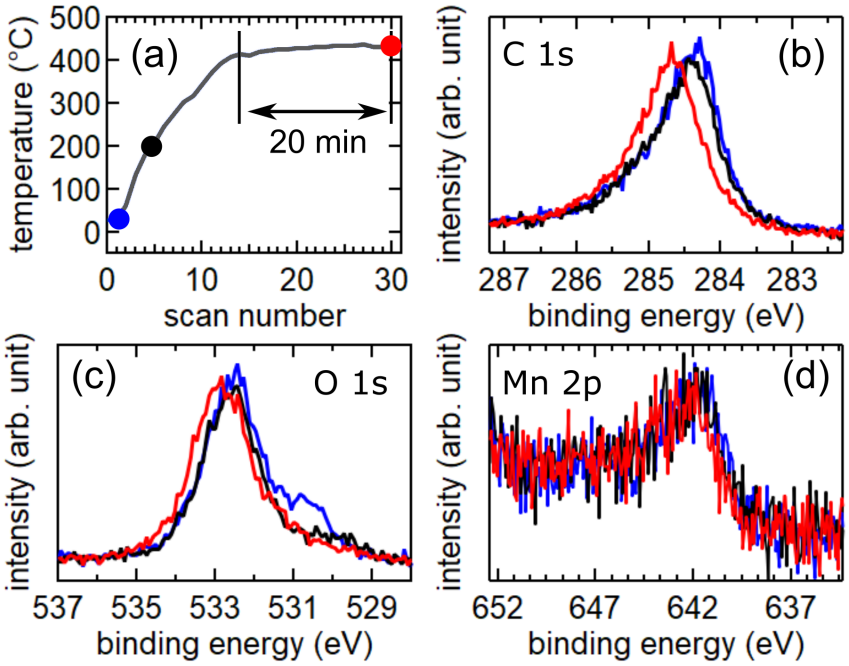

Figure 3: Real-time XPS data for Mn-implanted graphene on Cu(111). (a) Temperature ramp during heating and respective measurement scan number. The filled circles mark particularly relevant scans that are plotted in the other panels with the same color: as-implanted state at room temperature (blue), crossing 200 °C (black), after a nearly isothermal annealing in UHV at 425 °C for 20 min (red). XPS spectra near the following core-level peaks: (b) C 1s, (c) O 1s, (d) Mn $2p_{3/2}$.

high-resolution XPS measurements. As for the Mn $2p_{3/2}$ core-level peak (figure 3d), despite the low concentration of Mn ($\approx$ 2.3 % with respect to C atoms in monolayer graphene[8]) and the limited statistics of the real-time XPS measurements ($\approx$ 10 seconds per spectrum), we can observe that the peak area and the peak position are approximately constant during the entire annealing process, from the as-implanted to 425 °C annealed states. We note that the lower signal-to-noise ratio in the spectra of Mn-implanted graphene (figure 3) is due to the lower photoionization cross section (table 1). During real-time measurements, the photon energy cannot be changed (to adapt to the different core levels); therefore, one must use a photon energy that is high enough so that all the relevant cores levels can be measured. In this case, a higher photon energy (780 eV) was used for the measurements of the Mn-implanted sample to allow us to measure the Mn 2p core-level peak, located at BE $\approx$ 642 eV (figure 3d).

Based on the insight provided by the real-time XPS measurements into the compositional changes and core-level shifts of the C 1s and O 1s peaks up to 425 °C, we then selected relevant annealing temperatures for which to study these changes using high-resolution XPS measurements: 200 °C, 425 °C and 700 °C. Deconvolution of the C 1s core-level peak for pristine graphene (representative spectra shown in figure 4a, other spectra are shown in figure S2 of the supporting information) and Mn-implanted graphene (figure 4c) reveals two components related to graphitic carbon, at BE = 284.6 eV and at BE = 284.4 eV. The former matches with the expected peak position of graphene, where the observed charge transfer between graphene and Cu(111) (denoted as *coupled graphene*, to emphasize the graphene-Cu interaction) results in a core-level shift of +0.2 eV (BE = 284.6 eV) with respect to C signal measured in graphite (BE = 284.4 eV).[16,34–36] The latter is associated with a modified graphene-Cu interaction, with graphene remaining more charge-neutral. Such graphene-Cu decoupling has been associated with the partial oxidation of the underlying Cu(111), in the form of Cu_2O or CuO.[16] Formation of CuO can be excluded in the present case, based on the measurement of Cu 2p peak (*cf.* figure S3 in supporting information). Although

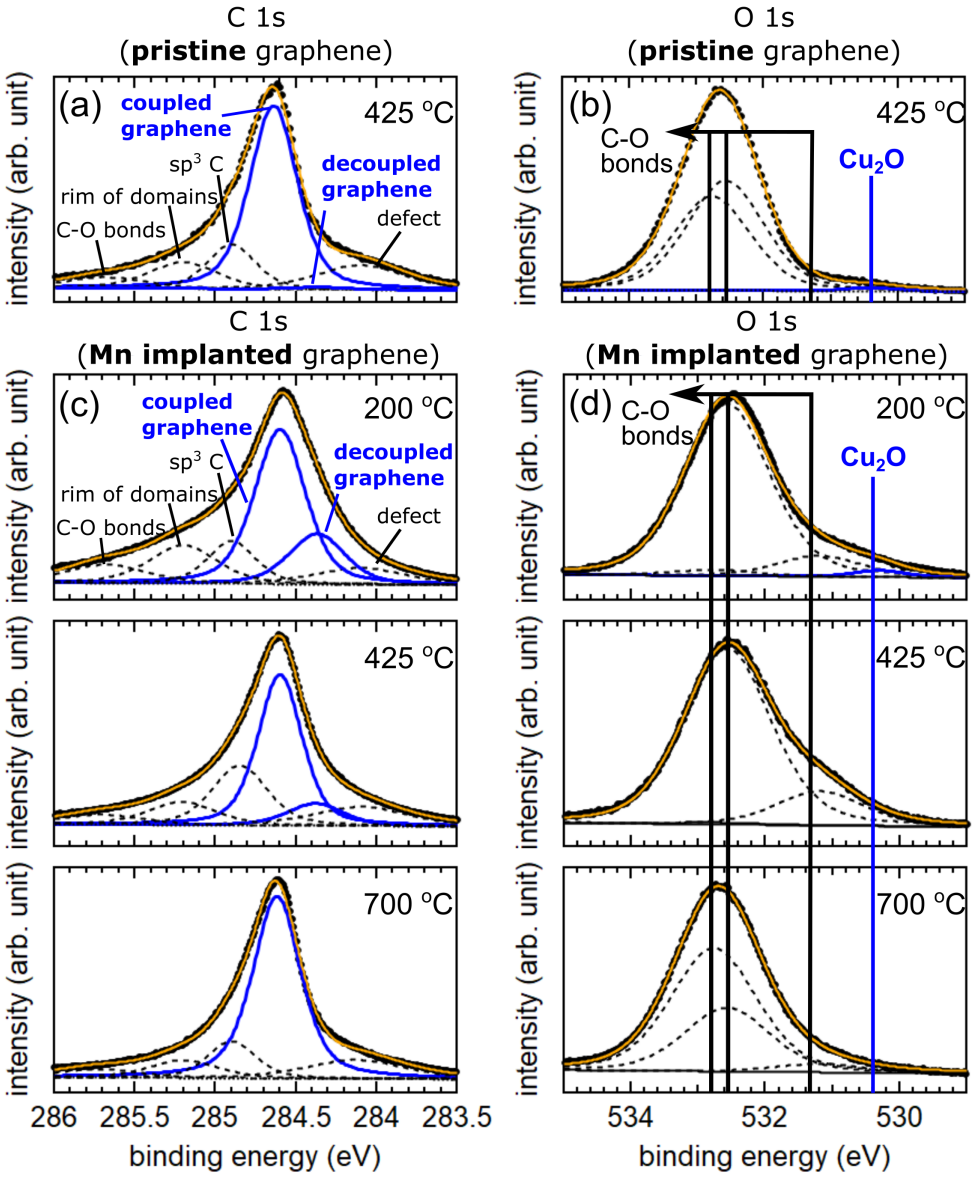

Figure 4: Deconvolution of C 1s (a, c) and O 1s (b, d) core-level peaks. (a, b) XPS spectra of pristine graphene on Cu(111), measured after annealing in UHV at 425 °C. (c, d) XPS spectra of Mn-implanted graphene on Cu(111), measured after annealing in UHV at (from top to bottom): 200 °C, 425 °C and 700 °C.

a Cu_2O component in the O 1s peak is observed, it is too small to be the sole origin of the decoupled graphene component, as we explain in more detail below when discussing the quantification as a function of annealing temperature (figure 5). Therefore, we refer to this C component as *decoupled graphene*, given the decrease or absence of graphene-Cu charge transfer, without establishing a direct relation with the Cu oxidation. Apart from the graphitic components, multiple peak components were also observed in the C 1s peak which can be assigned to contamination and disorder, including defects (*i.e.*, related to carbon vacancies, BE = 284.1 eV),[16] sp^3 carbon (BE = 284.9 eV),[16] the rims of the graphene domains (*i.e.*, domain boundaries, BE = 285.2 eV),[16] and various functional groups related to the bonding between C and O (*e.g.*, C-OH, C-O, C=O, etc.), which we refer to as C-O bonds (BE > 285.6 eV).[16,37,38] In order to further assess the origin of the weakened graphene-Cu interaction, we analyzed the O 1s core-level peak of pristine graphene (representative spectra shown in figure 4b, other spectra can be found in figures S1 and S2 of the supporting information) and Mn-implanted graphene (figure 4d). Two types of compounds can be identified: one related to the O 1s spectral component located at BE = 530.4 eV and another related to multiple peaks at BE > 531 eV. The former can be associated with Cu_2O[38] (consistent with the Cu 2p data), and the latter can be associated with the bonding between C and O in various functional groups (*e.g.*, C-OH, C-O, C=O, similar to the peak assignment of the C 1s peak).[16,37,38] From the deconvolution of the O 1s peak, we can see that there is virtually no trace (below detection limit) of Mn oxide present in our sample, namely MnO, Mn_2O_3, Mn_3O_4, MnO_2, which are all located at BE < 530 eV;[39–41] no peak component can be identified in this energy regime in our high-resolution data. Moreover, if we revisit the real-time XPS O 1s spectrum of Mn implanted graphene (figure 3c), although with relatively low resolution, it also indicates absence of peak components with BE < 530 eV, that is, no Mn oxide observed even in the as-implanted state. As for the real-time C 1s and O 1s spectra (figure 3), taking into consideration the more detailed insight provided by high-resolution results, we can conclude that the Mn implantation promotes the growth of Cu_2O;

annealing in UHV at 425 °C (for 20 minutes) decreases the Cu_2O component and induces a core-level shift of C 1s and O 1s peaks towards higher BE. For pristine graphene, the annealing process has little to no effect, since there is no detectable Cu_2O (*i.e.*, oxygen-free interface), even before annealing, that is, the pristine graphene layer efficiently protects the Cu surface. This is consistent with the notion that defects created in graphene by the Mn implantation decrease its efficiency in protecting the underlying Cu surface from oxidation. We note that the amount of oxide can vary from sample to sample, depending on the duration of exposure to air (in the order of tens of minutes). Nevertheless, our data shows that the oxidation of Cu(111) (formation of Cu_2O) in Mn-implanted graphene can be reversed by thermal annealing in UHV at 425 °C (20 minutes). These O atoms that are removed from the Cu_2O layer are likely to diffuse deeper into the Cu layer or be released into the vacuum through graphene defects that have not been annealed in the 425 °C step.

A more complete picture of the cleaning effect induced by annealing in UHV up to 700 °C is given in figure 5, where the peak area of the different components (from the high-resolution spectra shown in figure 4 and figure S2b in supporting information) is plotted as a function of annealing temperature. The ratio of the integrated areas of the decoupled-versus-coupled components (C 1s peak) shows a decrease with the sequential annealing steps. In particular, for Mn-implanted graphene, the ratio decreased from 0.35 to 0.18 between the 200 °C and 425 °C steps; after annealing in UHV at 700 °C, the ratio dropped to zero. However, the amount of Cu_2O component in the O 1s peak (figure 5), of the order of 1% with respect to C after annealing at 200 °C appears to be too small to be the sole origin of the decoupled graphene component (one order of magnitude higher). This strongly suggests that the observed decoupled fraction may also result from other effects that are induced or enhanced by the implantation and affected by thermal annealing: structural disorder in the graphene-Cu interface, Mn intercalation, and O-containing contaminants (intercalated at the graphene-Cu interface surface or incorporated in the Cu subsurface).

Whereas the graphitic components are related to (de)coupling effects, the other compo-

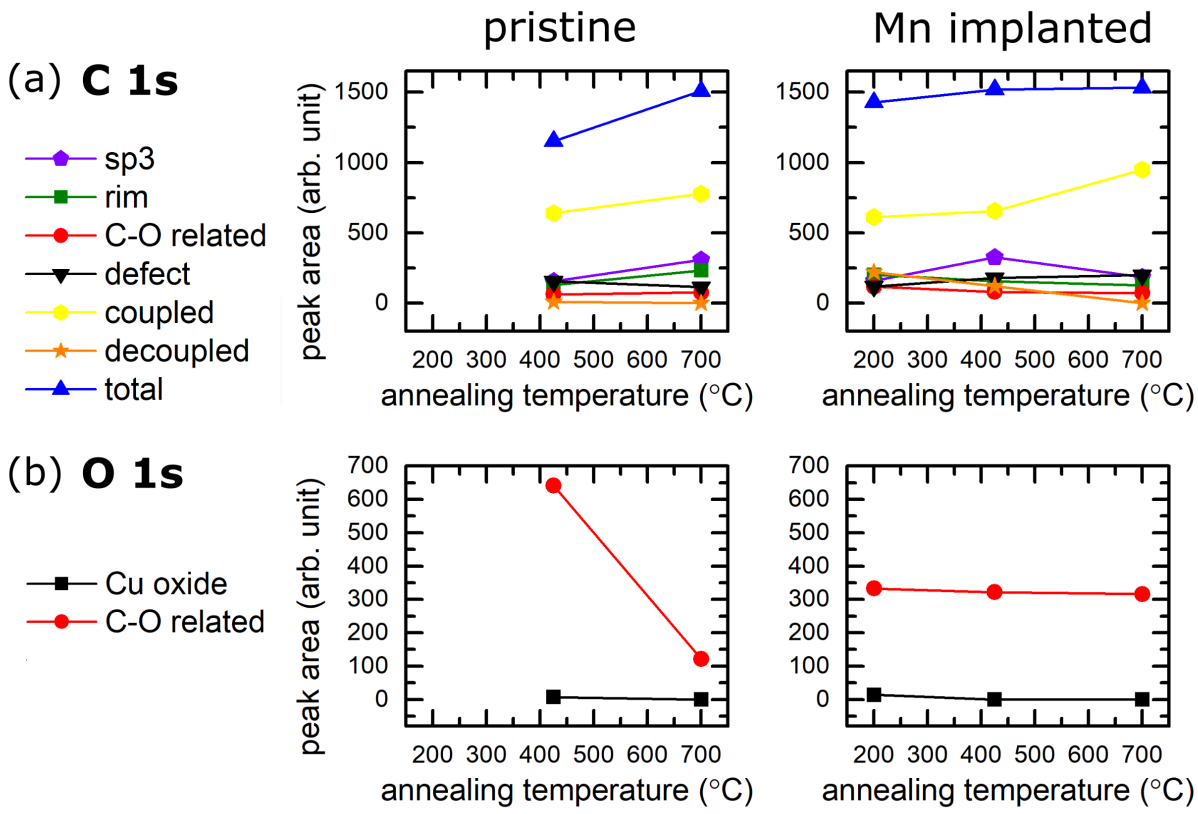

Figure 5: Integrated peak area of the components identified in the (a) C 1s and (b) O 1s core-level peaks, measured on pristine graphene on Cu(111) (left) and Mn-implanted graphene on Cu(111) (right), after annealing in UHV at 200 °C (only for Mn-implanted graphene, as described in the main text), 425 °C, and 700 °C.

nents of the C 1s peak provide information on contamination and disorder. Some of these non-graphitic components appear to decrease, as one would expect since UHV annealing should decrease the surface contamination and disorder. However some non-graphitic components actually appear to increase with increasing annealing temperature. The STM data, on the other hand, reveals a significant recovery already between the as-implanted state and the 425 °C annealing, as shown in figure 2c, where the only observable features correspond to substitutional Mn defects, strongly indicating that annealing in UHV indeed significantly decreases surface contamination and disorder, as expected. The increase in some of these non-graphitic components is thus likely only an apparent increase, resulting from the removal of surface contaminants, which increases the sensitivity to the C in graphene. This explanation is supported by the fact that the total C 1s peak area increases and the C-O related component of the O 1s peak (hydrocarbon contaminants) decreases, especially in the pristine sample. Two interesting differences between non-implanted and implanted graphene should be noted. First, after 425 °C annealing in UHV, the non-implanted graphene shows a significantly higher C-O related component in the O 1s spectrum compared to the implanted graphene. This C-O component is likely associated with contaminants on top of the graphene layer. The difference between pristine and implanted graphene may be simply related to different sample histories, in particular in terms of total ambient-exposure times between growth and annealing studies; it may also indicate that some surface contaminants are actually sputtered away during Mn implantation. Second, the cleaning effect induced in the Mn-implanted graphene (above 200 °C) is much weaker, virtually negligible up to 700 °C, remaining at approximately 20% O coverage with respect to C atoms in graphene.[8] The high thermal stability of this O-related contamination suggests stronger bonding to the graphene layer (*e.g.*, as a result of the ion irradiation) or even that they are underneath (*i.e.*, trapped by) the graphene layer. Moreover, since the STM data does not show such high concentrations of contaminants adsorbed on top of graphene (but instead an essentially contamination-free and well-ordered graphene surface), this O-related contamination

is likely intercalated between graphene and the Cu(111) surface or even incorporated in the (sub)surface of Cu. In the latter case (incorporated in the Cu (sub)surface), that would mean that part of the component identified as C-O-related in the XPS O 1s data (figure 4d) may in fact be associated with regions of non-stoichiometric Cu_xO underneath the graphene layer.

Annealing Effects on the Implanted Mn

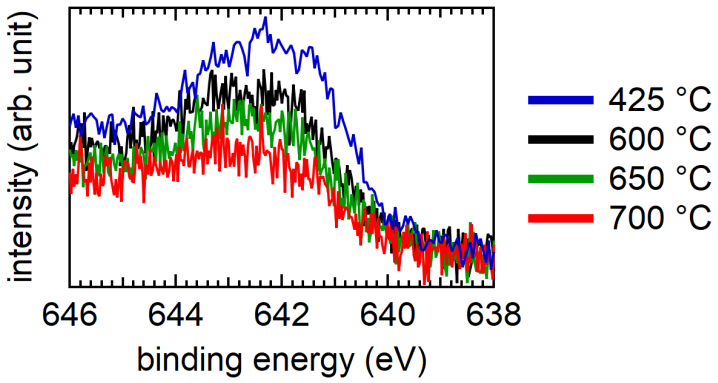

Figure 6: Mn $2p_{2/3}$ core-level spectrum of Mn-implanted graphene/Cu(111), annealed at the following temperatures after implantation: 425 °C (blue), 600 °C (black), 650 °C (green), and 700 °C (red).

Using a similar approach as in reference 8 to estimate the local concentration of substitutional Mn with respect to C atoms in graphene, based on the STM topographies, we obtain 0.04(±0.02)% after 425 °C, 0.04(±0.02)% after 525 °C and 0.07(±0.02)% after 700 °C. Within the standard deviation, the concentration of substitutional Mn is thus not significantly affected by thermal annealing, at least within the annealing temperature range for which the graphene surface is sufficiently clean and well-ordered to allow for a direct comparison (425-700 °C). This high thermal stability is quite remarkable, compared to other forms of covalent functionalization for which the bonds start to break at significantly lower temperatures (*e.g.,* 120 – 150 °C in reference 42). Obtaining detailed insight on the mechanism of formation of substitutional Mn is however very challenging, since it is not possible to perform a fully quantitative STM analysis of the as-implanted state nor for low annealing

temperatures. One can still hypothesize that there are two likely mechanisms: *direct substitution* in which the implanted Mn ion displaces a C atom and directly takes its position in the graphene lattice; *diffusion-assisted substitution* in which an implanted Mn ion becomes an adatom on top of graphene or an intercalated atom between graphene and the Cu surface, and then diffuses (in plane) until it becomes trapped in a C vacancy which had been created by that same Mn ion or any other. Gaining more insight on the relative importance of these two mechanisms would require a quantitative assessment (at the implantation temperature, *i.e.*, room temperature) of the amount and dynamics of the defects possibly involved in these processes (substitutional Mn, Mn adatoms, intercalated Mn, and C vacancies), which is however not possible with our STM data due to the disordered and contaminated surface in the as-implanted state. Whereas direct substitution is likely to be responsible for at least a fraction of the observed substitutional Mn defects, diffusion-assisted substitution may also be taking place (*i.e.*, cannot be excluded) even at room temperature, since the diffusion barrier of a Mn adatom on graphene is estimated to be extremely low (0.06 eV).[43] Mn adatoms (adsorbed upon implantation) may thus rapidly diffuse over the graphene surface, during the implantation under UHV, until they become trapped in a C vacancy,[44] which are likely to be much less mobile (the diffusion barrier of the C vacancy in graphene on Cu(111) is estimated to be 2.99 eV[45]). Once captured, the (substitutional) Mn atom has a strong binding to the C vacancy, as predicted by our previously reported DFT calculations, yielding a binding energy of -5.3 eV.[8] Not only does this high binding energy support the scenario of efficient trapping of diffusing Mn adatoms, it also explains why the substitutional Mn defect (regardless of its formation mechanism) has such a high thermal stability (at least up to 700 °C). Similar diffusion and trapping may also occur for Mn ions that become intercalated upon implantation; although we observe aggregation of such intercalated Mn atoms, as discussed below, it is possible that some of them also become trapped in C vacancies before aggregating, that is, also leading to diffusion-assisted substitution. Since both substitution mechanisms (direct or diffusion assisted) require that a C atom is removed from the graphene

lattice (to be replaced by Mn), it is relevant to discuss the minimal energy a Mn ion must have to create a stable C vacancy. To a first approximation, that minimal energy E_{min} can be estimated based on the binary collision approximation (BCA):[46]

$$E_{\mathrm{min}} = T_{\mathrm{d}} \frac{(M_{\mathrm{Mn}} + M_{\mathrm{C}})^2}{4 M_{\mathrm{Mn}} M_{\mathrm{C}}} \tag{1}$$

where T_{d} is the C threshold displacement energy (*i.e.*, minimum energy that must be transferred to the C atom to create a stable C vacancy), and M_{Mn} and M_{C} are the atomic masses of Mn and C, respectively. With $T_{\mathrm{d}} \approx 21$ eV,[9] equation 1 gives $E_{\mathrm{min}} \approx 36$ eV. However, such an estimation serves only as a rough guideline, since it does not account for chemical effects and for the role of the substrate (from which the displaced C atoms may recoil). Recent calculations based on density functional theory molecular dynamics (DFT-MD) predict E_{min} values that can strongly deviate from the BCA prediction.[46] Due to the low energy (compared to the higher energies for which BCA is more typically used) the collision, that is, the energy transfer between impinging and target atoms, takes a finite time, and therefore, chemical interactions between those atoms (and the energy involved) play a significant role.

As mentioned above, in addition to substitutional Mn, other forms of incorporation also occur (figure 1).[8] In particular, a large fraction, of the order of 50% of the implanted atoms are not incorporated at all.[8] This non-incorporated fraction is likely associated with backscattered Mn ions that are detected during the implantation since they deposit their charge when approaching the graphene layer; however they are backscattered, upon collision with atoms from the graphene layer or from the substrate, back into the vacuum.[8] Based on our data, we cannot exclude that a part of this non-incorporated fraction may consist of Mn atoms that were temporarily attached to the sample but experienced desorption at room temperature, before our XPS experiments. However, considering that calculated adsorption energies for Mn on graphene are of the order of several eV,[47] room temperature desorption can essentially be excluded. In any case, this non-incorporated component does not affect

further experiments or exploitation of these systems, and can be compensated by increasing the implanted fluence. There is however a large fraction, of the order of 50% of the Mn atoms, that are incorporated into the sample though not substitutionally.[8] This component consists of Mn atoms that are transmitted through the graphene layer (*e.g.*, by impinging in regions of lower energy barrier, *i.e.*, at the center of the C hexagon), and become intercalated into the graphene-substrate interface (figure 1b), or even incorporated into the substrate, forming a subsurface alloy (figure 1c). In previous work, it was observed that the amount of Mn incorporated in the sample (% with respect to C atoms in graphene) decreased upon annealing in UHV: from 2.3% after thermal annealing at 200 °C to 2.2% at 425 °C, and to 1.0% after annealing at 700 °C.[8] This decrease was interpreted as due to diffusion of the intercalated Mn atoms (figure 1b) into the Cu layer forming a subsurface alloy (figure 1b). In the present work, we further analyze the annealing temperature range between 425 °C and 700 °C, in order to understand whether an optimal annealing temperature regime exists, as a balance between the removal of non-substituted Mn and the annealing or creation of disorder (discussed in the next section). For that purpose, we carried out real-time XPS measurements. As can be seen in figure 6, the Mn signal already decreases after the 600 °C annealing in UHV, and keeps monotonously decreasing up to 700 °C. In good agreement with these XPS results, we identified with STM (figure 7) nanometer scale mounds that we ascribe to such non-substituted Mn (the non-implanted sample does not exhibit such mound objects). These mounds form at circular pit defects of the Cu surface. The atomic lattice of graphene can be resolved on top of these mounds indicating that they indeed consist of material intercalated between the substrate and graphene (inset in figure 7a). We see these Mn-related islands after annealing in UHV at 425 °C and up to 700 °C, at which point they become rare to find in the STM micrographs (figure 7b). We note that in both topographies (figure 7a,b) the substitutional Mn are resolved as randomly distributed protrusions, a smaller scale topography is shown in the inset of figure 7b to highlight the atomic structure of the substitutional Mn. More detailed STM studies would be necessary at lower

annealing temperatures to identify the temperature at which these Mn-related islands start to form. Nevertheless, based on these experimental observations, we can hypothesize that intercalated Mn atoms, which are implanted as a random distribution over the surface, first diffuse laterally (remaining intercalated) and form small Mn islands. These islands are likely nucleated in regions where intercalated Mn can be efficiently trapped, such as the pit defects of the Cu surface (figure 1b). Subsequently, at higher annealing temperatures, intercalated Mn diffuses into the Cu layer forming a subsurface alloy (figure 1c). The formation of such a subsurface alloy has indeed been predicted to be thermodynamically favorable compared to the intercalated Mn layer configuration, in graphene on Cu(111).[48] The diffusion of Mn into Cu, towards the alloy formation, is likely to be associated with a high diffusion barrier, requiring relatively high annealing temperatures (above 425 °C). Although the Mn atoms remain in the sample, their apparent intensity decreases in our XPS data, due to inelastic scattering of the photoelectrons, as the Mn atoms diffuse into Cu with increasing annealing temperature (diffusion of a larger fraction of the Mn atoms, and deeper into the Cu layer). The peak shape does not significantly change, which is consistent with the notion that the signal is dominated by the intercalated Mn and subsurface alloy, with similar spectral signatures. A more detailed analysis, that is, resolving different components as we performed for the C and O 1s spectra, is significantly more challenging and ambiguous for the Mn 2p core-level spectra. Nevertheless, our analysis of the O 1s core-level peak (no peak component with BE $<$ 530 eV) strongly suggests that a Mn-oxide component, if at all present, would be negligible. This indicates that the probability for Mn adsorption (on top of the graphene layer) during implantation is negligible compared to intercalation and backscattering; otherwise, since adsorbed Mn is not protected against oxidation, it would contribute to the spectra as a Mn-oxide component.[49] As discussed above, it is also possible that Mn atoms that are adsorbed during the implantation become substitutional via a diffusion-assisted process; nevertheless, this still constitutes a small fraction compared to intercalated and backscattered Mn components.

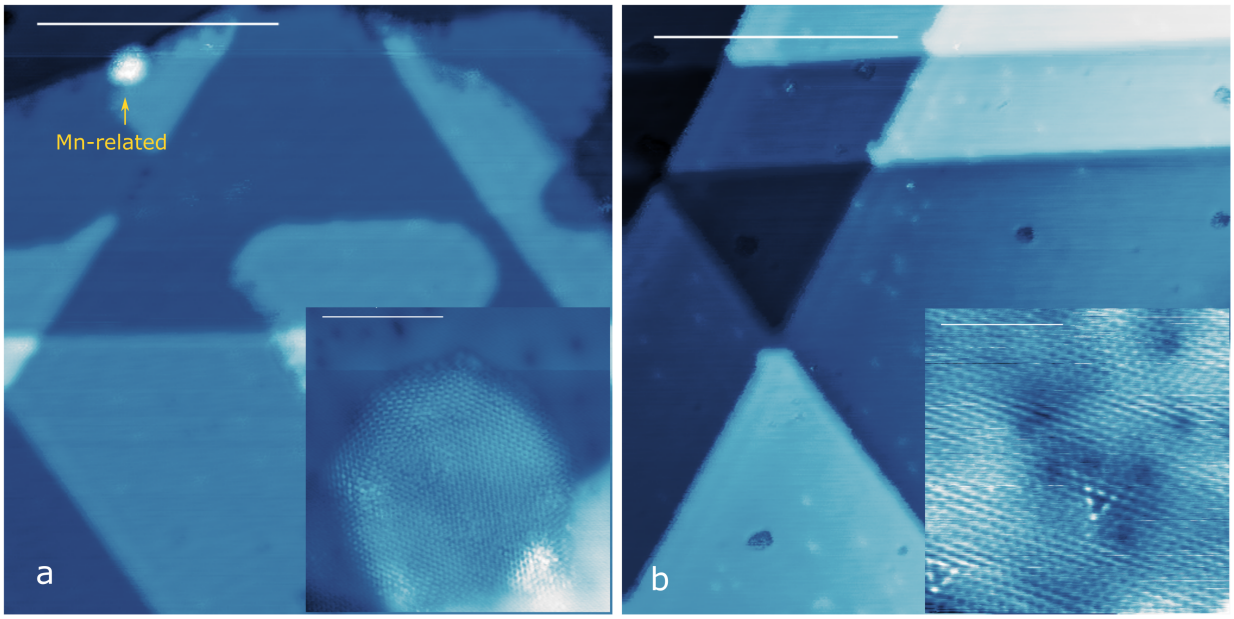

Figure 7: STM topographies of graphene on Cu(111) implanted with Mn. (a) Annealed to 525 °C (scale bar: 20 nm, V_{sample} = - 200 mV, $I_{\text{tun.}}$ = 700 pA). Inset shows the detail of the surface structure on a Mn-related island (scale bar: 4 nm, V_{sample} = - 100 mV, $I_{\text{tun.}}$ = 3 nA). (b) Annealed to 700 °C (scale bar: 20 nm, V_{sample} = 100 mV, $I_{\text{tun.}}$ = 400 pA). Inset shows the detail of a substitutional Mn (scale bar: 2 nm, V_{sample} = - 100 mV, $I_{\text{tun.}}$ = 1 nA).

Annealing of Implantation-Induced Disorder

Although the XPS and STM data presented above provide some insight into defect formation upon implantation and recovery upon annealing in UHV, that information can be ambiguous (and very local in the case of STM). We used Raman spectroscopy to more directly and quantitatively characterize the implantation-induced disorder and its thermal annealing. The Raman spectra in figure 8 were measured at room temperature in the as-implanted state and after thermal annealing in UHV at 200 °C, 425 °C, 525 °C, 610 °C, and 700 °C. In the as-implanted state (figure 8b), the spectrum features four Raman bands (*D*, *G*, *D′* and *2D* bands). These Raman bands can be divided in two different categories: *G* and *2D* bands are associated with the graphene sp^2 bond; *D* and *D′* bands are activated by disorder. For both disorder-related bands, the peak intensity decreases with increasing annealing temperature. Already after annealing in UHV at 525 °C (figure 8e), the intensity of the *D′* band has been strongly reduced, coming close to the noise level. The intensity of the *D* band also decreases

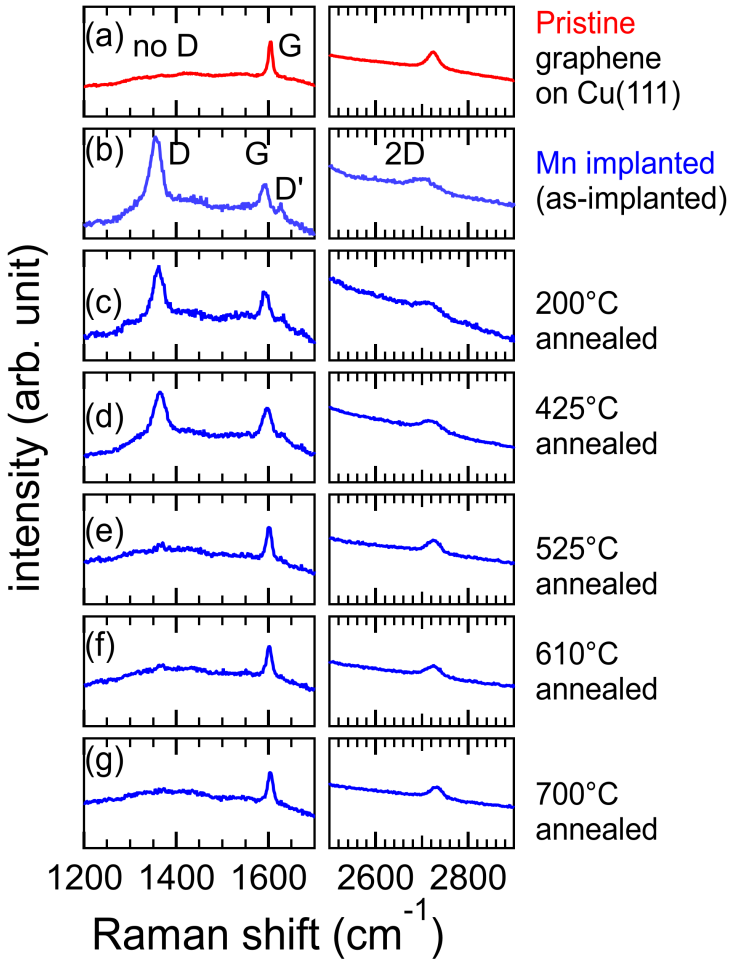

Figure 8: Raman spectra of pristine graphene on Cu(111) (a) and Mn-implanted graphene on Cu(111) (b-g), measured as a function of annealing temperature. From top to bottom: as-implanted state (b); and measured after annealing in UHV at 200 °C (c); 425 °C (d); 525 °C (e); 610 °C (f); 700 °C (g). The positions of the *D*, *G*, *D′* and *2D* bands of graphene are labeled in panel (b). The intensity of the spectra (on both left and right panels) is normalized to the intensity of the corresponding *G* bands. The data shown on the right and left panels are part of the same spectrum; the range in the intensity axis on the right panel is shifted vertically with respect to the plot on the left panel but they have the same scaling (same interval in intensity).

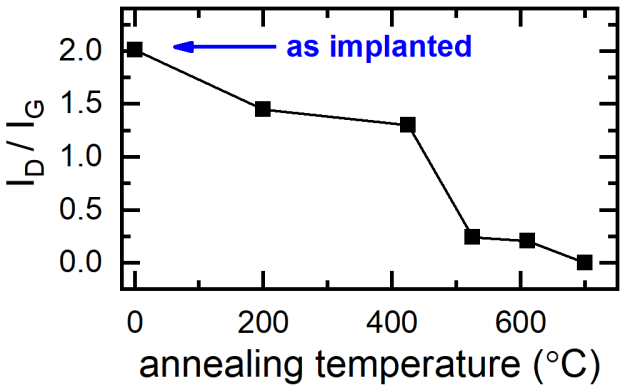

Figure 9: D band *versus* G band intensity ratio of Mn-implanted graphene on Cu(111), as a function of annealing temperature.

at 525 °C and is undetectable after annealing in UHV at 700 °C (figure 8g), with the Raman spectrum becoming essentially indistinguishable from that of pristine graphene (figure 8a). In figure 9, we plot the ratio between the intensities of the D band and the G band (I_D/I_G), as a function of annealing temperature. From the as-implanted state up to 425 °C, I_D/I_G gradually decreases from 2.01 to 1.30. It is possible that the surface cleaning and Cu_2O removal (discussed above based on the STM and XPS data) plays a role in this decrease in disorder (*e.g.,* covalently bonded hydrocarbons being removed, allowing for recovery of sp^2 bonding in those regions). At 525 °C, the I_D/I_G ratio drops dramatically from 1.30 to 0.24, indicating an almost complete recovery of the graphene lattice. Above 525 °C, that is, at 610 °C and 700 °C, the D band intensity continues to decrease, and becomes lower than the detection limit ($I_D/I_G \sim 0.15$, for measurements on graphene on Cu(111) with low defect density, *i.e., stage 1* of the amorphization trajectory[50]). This evolution with annealing temperature shows the same trend as recently reported,[8] where Raman spectroscopy measurements were reported for the as-implanted state and after annealing in UHV at 700 °C in a sample prepared under similar conditions (more details in section *Reproducibility of the Raman characterization* of the supporting information). Although such a decrease in disorder can be expected, thermal annealing may in general induce more complex phenomena. For example, thermal annealing of ion irradiated h-BN was observed to result in the formation of holes in the h-BN layer, which is understood as due to vacancies (created upon irradiation)

that propagate along the rim of a nanomesh pore during annealing.[51] In short, our Raman spectroscopy data shows that significant recovery from the implantation-induced disorder requires thermal annealing in UHV at least at 525 °C. Annealing in UHV at 700 °C restored implanted graphene to a nearly pristine state from the perspective of Raman spectroscopy. In agreement with this observation, STM also shows a well-ordered graphene lattice (with substitutional Mn atoms) and graphene-Cu(111) interface, similar to non-implanted samples (including a visible moiré superstructure - figure 2a,c).

Band Structure

We further investigated the effect of thermal annealing in UHV on both pristine and Mn-implanted graphene on Cu(111) using angle-resolved photoemission spectroscopy (ARPES). Not only do these measurements allow us to characterize how the implantation and annealing affects the electronic band structure of this particular system, they also provide general guidelines for other studies on ULE-implanted graphene using photoemission techniques. We performed a more detailed annealing study on non-implanted graphene on Cu(111) (*i.e.*, more annealing steps in the low-temperature range), as it provides a more unambiguous interpretation of the results. In implanted graphene, both surface contamination and implantation-induced disorder can contribute to the weakening or even non-observability of bands, whereas in a non-implanted, highly-ordered graphene, only contamination should play a role. We focused on measurements near the Dirac cone of graphene, as they allow to determine important parameters, for example, the Fermi-level position with respect to the Dirac point, the gap opening induced by the hybridization between Cu 3d and graphene π states[8,35,52] and other modifications of the Dirac-like behavior of functionalized graphene.

Figure 10 shows the ARPES spectra of pristine graphene on Cu(111), measured close to the K point of the first surface Brillouin zone, where the Dirac cone is located. The UHV annealing was carried out in four steps: 250 °C, 350 °C, 425 °C, and 700 °C. After the first step (250 °C, figure 10a), no band structure can be identified. After the second step

(350 °C, figure 10b), a very faint Dirac cone starts appearing. After the third step (425 °C, figure 10c), the Dirac cone became clearly visible. However, the signal-to-noise ratio remains too low, unsuitable for a proper fitting of the energy distribution curves (EDC). Therefore, one can only estimate the Dirac point position by finding the lowest intensity point at K point (BE = 0.29 eV), and it is not possible to determine the gap opening around the Dirac point. After the last step (700 °C, figure 10d), the background is further suppressed, and the spectral intensity significantly enhanced. This is consistent with the further cleaning of the graphene surface after the annealing in UHV at 700 °C, observed in the XPS data (figure 5). The EDC fitting yields a Dirac point located at BE = 0.33(1) eV and a gap opening of 0.40(2) eV, as previously reported.[8]

For Mn-implanted graphene (figure 11), the data after annealing in UHV at 425 °C and 700 °C is qualitatively similar to pristine graphene, that is, improving from a visible though low-contrast Dirac cone (425 °C) to a high-quality spectrum with high spectral intensity and low background (700 °C). However, since our XPS data shows no significant cleaning between these annealing steps, this improvement is more likely related to other modifications. In particular, the significant decrease in graphene disorder (observed in the Raman study, figure 9) can be expected to produce such improvement in the spectral features. Going in more detail into band structure parameters, after the annealing in UHV at 425 °C (figure 11a), the Dirac point position is found at approximately BE = 0.52 eV, estimated as the lowest intensity point near the Dirac point; a proper EDC analysis cannot be performed due to low signal-to-noise ratio. This significantly improves after the annealing in UHV at 700 °C (figure 11b) and EDC analysis yields a Dirac point located at BE = 0.43(1) eV and the gap opening of 0.23(2) eV as previously reported.[8] Comparing the Dirac point position measured at 425 °C and 700 °C yields a BE shift of approximately -0.09 eV. However, since various factors that influence the Fermi level in graphene change upon annealing in UHV (graphene defects, contaminants/impurities, non-substitutional Mn configurations), it is not possible to establish the origin of this shift based on the present data. We can nevertheless

note that an intercalated Mn layer, between graphene and Cu(111), has been predicted to destroy the Dirac cone, while a subsurface alloy preserves it.[48] The conversion from intercalated Mn to subsurface alloy (indicated by our XPS and STM data, as discussed above) may therefore also contribute, together with the disorder annealing, to the improvement in the spectral features observed in the ARPES data from 425 °C to 700 °C annealing in UHV.

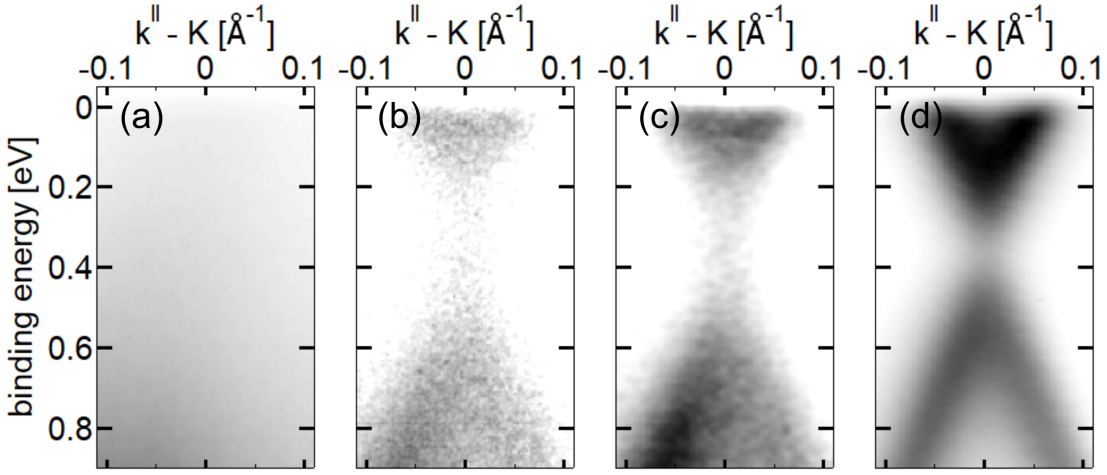

Figure 10: ARPES spectra (hν = 34 eV) of pristine graphene on Cu(111) after annealing in UHV at 250 °C (a), 350 °C (b), 425 °C (c), and 700 °C (d), measured near the K point along the $\Gamma \rightarrow K$ direction. Panel (d) corresponds to the annealing step reported in reference 8.

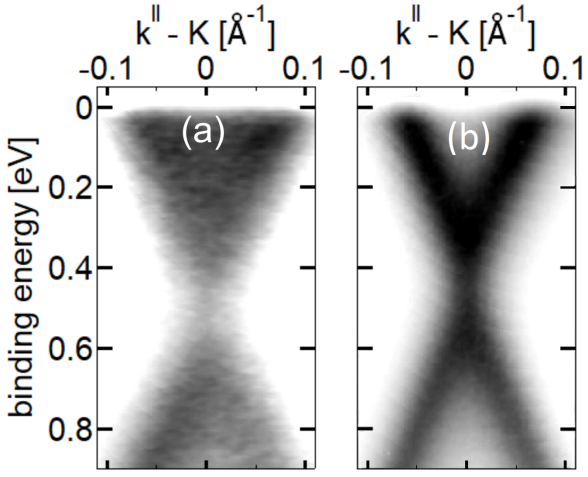

Figure 11: ARPES spectra (hν = 34 eV) of Mn-implanted graphene on Cu(111) after annealing in UHV at 425 °C (a) and 700 °C (b), measured near the K point along the $\Gamma \rightarrow K$ direction. Panel (b) corresponds to the annealing step reported in reference 8.

Conclusions

We studied the effect of thermal annealing in UHV on epitaxial graphene grown on Cu(111) and implanted with Mn at 40 eV, to a fluence of 1.5×10^{14} ions per cm^2. In particular, using STM, Raman spectroscopy and synchrotron-based XPS and ARPES, we studied the evolution of the surface contamination and of the implantation-induced disorder. While significant surface cleaning occurred at annealing temperatures as low as 200 °C, damage recovery was relatively limited even up to 400 °C. Significant recovery required thermal annealing in UHV at least at 525 °C. Annealing in UHV at 700 °C restored implanted graphene to a nearly pristine state. Such high temperature annealing, in the 600-700 °C range also results in a decrease in the amount of Mn at the surface which indicates that the Mn atoms that were incorporated as intercalated species (between graphene and the Cu surface) upon implantation experience diffusion into the Cu layer, creating a subsurface alloy.

In short, our results show that optimal annealing is achieved at temperatures around 700 °C. In particular, STM shows a well-ordered graphene lattice, on a flat, nearly featureless surface, that is, similar to pristine graphene although with the added substitutional Mn atoms. ARPES measurements reveal a well-defined Dirac cone, comparable to pristine graphene, with only minor modifications likely induced by substitutional Mn and other implantation-induced effects (*e.g.,* non-substitutional Mn and lattice defects, although these are minimized upon 700 °C annealing in UHV). The surface cleaning resulting from thermal annealing at 425 °C in UHV allows to probe the band structure by decreasing the detrimental photoelectron scattering from contaminants. The improvement in the ARPES spectral features between 425 °C and 700 °C annealing in UHV is likely due to further annealing of defects, that is, the recovery of a highly-ordered lattice structure restores the well-defined band structure.

These results also set useful guidelines for future experimental studies on ULE-implanted graphene, in particular based on widely-used techniques such as scanning probe microscopies

and photoemission spectroscopies. In particular, while it is possible to perform STM measurements on as-implanted graphene, thermal annealing in UHV at least at 425 °C makes it significantly easier to probe the substitutional dopants. On the other hand, while the Dirac cone can be observed after annealing in UHV at 425 °C, the quality of the ARPES data (and therefore the amount or precision of band-structure parameters that can be extracted) significantly increases after annealing in UHV at 700 °C.

Supporting Information Available

The Supporting Information is available free of charge at ...

- Additional XPS details and results with accompanying references[53,54]
- Reproducibility of the Raman characterization
- LEED characterization

Acknowledgement

This work was funded by KU Leuven and FWO Vlaanderen. The authors acknowledge Elettra Sincrotrone Trieste for providing access to its synchrotron radiation facilities and, in particular, to the BaDElPh and SuperESCA beamlines. The access to the Elettra Sincrotrone Trieste has been supported by the project CALIPSOplus under Grant Agreement 730872 from the EU Framework Programme for Research and Innovation HORIZON 2020. The authors also thank Peter Walke for the support with the Raman spectroscopy measurements.

References

(1) Bangert, U.; Pierce, W.; Kepaptsoglou, D.; Ramasse, Q.; Zan, R.; Gass, M.; Van den Berg, J.; Boothroyd, C.; Amani, J.; Hofsässs, H. Ion Implantation of Graphene - Toward IC Compatible Technologies. *Nano Lett.* **2013**, *13*, 4902–4907.

(2) Willke, P.; Amani, J.; Thakur, S.; Weikert, S.; Druga, T.; Maiti, K.; Hofsäss, H.; Wenderoth, M. Short-Range Ordering of Ion-Implanted Nitrogen Atoms in SiC-Graphene. *Appl. Phys. Lett.* **2014**, *105*, 111605.

(3) Kepaptsoglou, D.; Hardcastle, T. P.; Seabourne, C. R.; Bangert, U.; Zan, R.; Amani, J. A.; Hofsäss, H.; Nicholls, R. J.; Brydson, R. M. D.; Scott, A. J. et al. Electronic Structure Modification of Ion Implanted Graphene: The Spectroscopic Signatures of *p*- and *n*-Type Doping. *ACS Nano* **2015**, *9*, 11398–11407.

(4) Willke, P.; Amani, J. A.; Sinterhauf, A.; Thakur, S.; Kotzott, T.; Druga, T.; Weikert, S.; Maiti, K.; Hofsäss, H.; Wenderoth, M. Doping of Graphene by Low-Energy Ion Beam Implantation: Structural, Electronic, and Transport Properties. *Nano Lett.* **2015**, *15*, 5110–5115.

(5) Cress, C. D.; Schmucker, S. W.; Friedman, A. L.; Dev, P.; Culbertson, J. C.; Lyding, J. W.; Robinson, J. T. Nitrogen-Doped Graphene and Twisted Bilayer Graphene *via* Hyperthermal Ion Implantation with Depth Control. *ACS Nano* **2016**, *10*, 3714–3722.

(6) Susi, T.; Hardcastle, T. P.; Hofsäss, H.; Mittelberger, A.; Pennycook, T. J.; Mangler, C.; Drummond-Brydson, R.; Scott, A. J.; Meyer, J. C.; Kotakoski, J. Single-Atom Spectroscopy of Phosphorus Dopants Implanted into Graphene. *2D Mater.* **2017**, *4*, 021013.

(7) Tripathi, M.; Markevich, A.; Bottger, R.; Facsko, S.; Besley, E.; Kotakoski, J.; Susi, T. Implanting Germanium into Graphene. *ACS Nano* **2018**, *12*, 4641–4647.

(8) Lin, P.-C.; Villarreal, R.; Achilli, S.; Bana, H.; Nair, M. N.; Tejeda, A.; Verguts, K.; De Gendt, S.; Auge, M.; Hofsäss, H. et al. Doping Graphene with Substitutional Mn. *ACS Nano* **2021**, *15*, 5449–5458.

(9) Susi, T.; Hofer, C.; Argentero, G.; Leuthner, G. T.; Pennycook, T. J.; Mangler, C.; Meyer, J. C.; Kotakoski, J. Isotope Analysis in the Transmission Electron Microscope. *Nat. Commun.* **2016**, *7*, 13040.

(10) Åhlgren, E. H.; Kotakoski, J.; Krasheninnikov, A. Atomistic Simulations of the Implantation of Low-Energy Boron and Nitrogen Ions into Graphene. *Phys. Rev. B* **2011**, *83*, 115424.

(11) Lehtinen, O.; Kotakoski, J.; Krasheninnikov, A.; Tolvanen, A.; Nordlund, K.; Keinonen, J. Effects of Ion Bombardment on a Two-Dimensional Target: Atomistic Simulations of Graphene Irradiation. *Phys. Rev. B* **2010**, *81*, 153401.

(12) Åhlgren, E.; Kotakoski, J.; Lehtinen, O.; Krasheninnikov, A. Ion Irradiation Tolerance of Graphene as Studied by Atomistic Simulations. *Appl. Phys. Lett.* **2012**, *100*, 233108.

(13) Kretschmer, S.; Maslov, M.; Ghaderzadeh, S.; Ghorbani-Asl, M.; Hlawacek, G.; Krasheninnikov, A. V. Supported Two-Dimensional Materials under Ion Irradiation: The Substrate Governs Defect Production. *ACS Appl. Mater. Interfaces* **2018**, *10*, 30827–30836.

(14) Li, Z.; Wang, Y.; Kozbial, A.; Shenoy, G.; Zhou, F.; McGinley, R.; Ireland, P.; Morganstein, B.; Kunkel, A.; Surwade, S. P. et al. Effect of Airborne Contaminants on the Wettability of Supported Graphene and Graphite. *Nat. Mater.* **2013**, *12*, 925–931.

(15) Wlasny, I.; Dabrowski, P.; Rogala, M.; Kowalczyk, P. J.; Pasternak, I.; Strupinski, W.; Baranowski, J.; Klusek, Z. Role of Graphene Defects in Corrosion of Graphene-Coated Cu(111) Surface. *Appl. Phys. Lett.* **2013**, *102*, 111601.

(16) Blume, R.; Kidambi, P. R.; Bayer, B. C.; Weatherup, R. S.; Wang, Z.-J.; Weinberg, G.; Willinger, M.-G.; Greiner, M.; Hofmann, S.; Knop-Gericke, A. et al. The Influence of Intercalated Oxygen on the Properties of Graphene on Polycrystalline Cu under Various Environmental Conditions. *Phys. Chem. Chem. Phys* **2014**, *16*, 25989–26003.

(17) Li, Z.; Li, S.; Chen, H.-Y. T.; Gao, N.; Schouteden, K.; Qiang, X.; Zhao, J.; Brems, S.; Huyghebaert, C.; Van Haesendonck, C. Strongly Hole-Doped and Highly Decoupled Graphene on Platinum by Water Intercalation. *J. Phys. Chem. Lett.* **2019**, *10*, 3998–4002.

(18) Sun, P.; Yang, Q.; Kuang, W.; Stebunov, Y.; Xiong, W.; Yu, J.; Nair, R. R.; Katsnelson, M.; Yuan, S.; Grigorieva, I. et al. Limits on Gas Impermeability of Graphene. *Nature* **2020**, *579*, 229–232.

(19) Verguts, K.; Schouteden, K.; Wu, C.-H.; Peters, L.; Vrancken, N.; Wu, X.; Li, Z.; Erkens, M.; Porret, C.; Huyghebaert, C. et al. Controlling Water Intercalation is Key to a Direct Graphene Transfer. *ACS Appl. Mater. Interfaces* **2017**, *9*, 37484–37492.

(20) Gottardi, S.; Müller, K.; Bignardi, L.; Moreno-López, J. C.; Pham, T. A.; Ivashenko, O.; Yablonskikh, M.; Barinov, A.; Björk, J.; Rudolf, P. et al. Comparing Graphene Growth on Cu(111) *versus* Oxidized Cu(111). *Nano Lett.* **2015**, *15*, 917–922.

(21) Lin, Y.-C.; Lu, C.-C.; Yeh, C.-H.; Jin, C.; Suenaga, K.; Chiu, P.-W. Graphene Annealing: How Clean Can It Be? *Nano Lett.* **2012**, *12*, 414–419.

(22) Siokou, A.; Ravani, F.; Karakalos, S.; Frank, O.; Kalbac, M.; Galiotis, C. Surface Refinement and Electronic Properties of Graphene Layers Grown on Copper Substrate: An XPS, UPS and EELS Study. *Appl. Surf. Sci.* **2011**, *257*, 9785–9790.

(23) Zion, E.; Butenko, A.; Kaganovskii, Y.; Richter, V.; Wolfson, L.; Sharoni, A.; Kogan, E.; Kaveh, M.; Shlimak, I. Effect of Annealing on Raman Spectra of Monolayer Graphene Samples Gradually Disordered by Ion Irradiation. *J. Appl. Phys.* **2017**, *121*, 114301.

(24) Verguts, K.; Vrancken, N.; Vermeulen, B.; Huyghebaert, C.; Terryn, H.; Brems, S.; De Gendt, S. Single-layer Graphene Synthesis on a Al_2O_3(0001)/Cu(111) Template Using Chemical Vapor Deposition. *ECS J. Solid State Sci. Technol.* **2016**, *5*, Q3060.

(25) Hofsäss, H.; Binder, H.; Klumpp, T.; Recknagel, E. Doping and Growth of Diamond-Like Carbon Films by Ion Beam Deposition. *Diamond Relat. Mater.* **1994**, *3*, 137–142.

(26) Junge, F.; Auge, M.; Hofsäss, H. Sputter Hot Filament Hollow Cathode Ion Source and Its Application to Ultra-Low Energy Ion Implantation in 2D Materials. *Nucl. Instrum. Methods Phys. Res. B: Beam Interact. Mater. At.* **2022**, *510*, 63–68.

(27) Petaccia, L.; Vilmercati, P.; Gorovikov, S.; Barnaba, M.; Bianco, A.; Cocco, D.; Masciovecchio, C.; Goldoni, A. BaD ElPh: A 4 m Normal-Incidence Monochromator Beamline at Elettra. *Nucl. Instrum. Methods. Phys. Res. B* **2009**, *606*, 780–784.

(28) Bartels, L.; Meyer, G.; Rieder, K.-H. The evolution of CO adsorption on Cu (111) as studied with bare and CO-functionalized scanning tunneling tips. *Surf. Sci.* **1999**, *432*, L621–L626.

(29) Hollen, S.; Tjung, S.; Mattioli, K.; Gambrel, G.; Santagata, N.; Johnston-Halperin, E.; Gupta, J. Native Defects in Ultra-High Vacuum Grown Graphene Islands on Cu (1 1 1). *J. Condens. Matter Phys.* **2015**, *28*, 034003.

(30) Tjung, S.; Hollen, S.; Gambrel, G.; Santagata, N.; Johnston-Halperin, E.; Gupta, J. Crystalline Hydrogenation of Graphene by Scanning Tunneling Microscope Tip-Induced Field Dissociation of H_2. *Carbon* **2017**, *124*, 97–104.

(31) Wiame, F.; Maurice, V.; Marcus, P. Initial Stages of Oxidation of Cu (1 1 1). *Surf. Sci.* **2007**, *601*, 1193–1204.

(32) Phillipson, R.; De La Rosa, C. J. L.; Teyssandier, J.; Walke, P.; Waghray, D.; Fujita, Y.; Adisoejoso, J.; Mali, K. S.; Asselberghs, I.; Huyghebaert, C. et al. Tunable Doping of

Graphene by Using Physisorbed Self-Assembled Networks. *Nanoscale* **2016**, *8*, 20017–20026.

(33) Yeh, J.; Lindau, I. Atomic Subshell Photoionization Cross Sections and Asymmetry Parameters. *At. Data Nucl. Data Tables* **1985**, *32*, 1 – 155.

(34) Balasubramanian, T.; Andersen, J.; Wallden, L. Surface-Bulk Core-Level Splitting in Graphite. *Phys. Rev. B* **2001**, *64*, 205420.

(35) Avila, J.; Razado, I.; Lorcy, S.; Fleurier, R.; Pichonat, E.; Vignaud, D.; Wallart, X.; Asensio, M. C. Exploring Electronic Structure of One-Atom Thick Polycrystalline Graphene Films: A Nano Angle Resolved Photoemission Study. *Sci. Rep.* **2013**, *3*, 2439.

(36) Tatti, R.; Aversa, L.; Verucchi, R.; Cavaliere, E.; Garberoglio, G.; Pugno, N. M.; Speranza, G.; Taioli, S. Synthesis of Single Layer Graphene on Cu(111) by C_{60} Supersonic Molecular Beam Epitaxy. *RSC Adv.* **2016**, *6*, 37982–37993.

(37) Kwak, J.; Jo, Y.; Park, S.-D.; Kim, N. Y.; Kim, S.-Y.; Shin, H.-J.; Lee, Z.; Kim, S. Y.; Kwon, S.-Y. Oxidation Behavior of Graphene-Coated Copper at Intrinsic Graphene Defects of Different Origins. *Nat. Commun.* **2017**, *8*, 1549.

(38) Ghijsen, J.; Tjeng, L.-H.; van Elp, J.; Eskes, H.; Westerink, J.; Sawatzky, G. A.; Czyzyk, M. T. Electronic Structure of Cu_2O and CuO. *Phys. Rev. B* **1988**, *38*, 11322.

(39) Rosso, J. J.; Hochella Jr, M. F. Natural Iron and Manganese Oxide Samples by XPS. *Surf. Sci. Spectra* **1996**, *4*, 253–265.

(40) Strohmeier, B. R.; Hercules, D. M. Surface Spectroscopic Characterization of Manganese/Aluminum Oxide Catalysts. *J. Phys. Chem.* **1984**, *88*, 4922–4929.

(41) Biesinger, M. C.; Payne, B. P.; Grosvenor, A. P.; Lau, L. W.; Gerson, A. R.; Smart, R. S. C. Resolving Surface Chemical States in XPS Analysis of First Row Transition

Metals, Oxides and Hydroxides: Cr, Mn, Fe, Co and Ni. *Appl. Surf. Sci.* **2011**, *257*, 2717–2730.

(42) Van Gorp, H.; Walke, P.; Teyssandier, J.; Hirsch, B. E.; Uji-i, H.; Tahara, K.; Tobe, Y.; Van der Auweraer, M.; De Feyter, S. On the Thermal Stability of Aryl Groups Chemisorbed on Graphite. *J. Phys. Chem. C.* **2019**, *124*, 1980–1990.

(43) Liu, X.; Wang, C.-Z. Growth Mode and Structures of Magnetic Mn Clusters on Graphene. *RSC Adv.* **2016**, *6*, 64595–64604.

(44) Liu, Y.; Liu, X.; Wang, C.-Z.; Han, Y.; Evans, J. W.; Lii-Rosales, A.; Tringides, M. C.; Thiel, P. A. Mechanism of Metal Intercalation under Graphene through Small Vacancy Defects. *J. Phys. Chem. C.* **2021**, *125*, 6954–6962.

(45) Wang, L.; Zhang, X.; Chan, H. L.; Yan, F.; Ding, F. Formation and Healing of Vacancies in Graphene Chemical Vapor Deposition (CVD) Growth. *J. Am. Chem. Soc.* **2013**, *135*, 4476–4482.

(46) Kretschmer, S.; Ghaderzadeh, S.; Facsko, S.; Krasheninnikov, A. V. Threshold Ion Energies for Creating Defects in 2D Materials from First-Principles Calculations: Chemical Interactions Are Important. *J. Phys. Chem. Lett.* **2022**, *13*, 514.

(47) Anithaa, V.; Shankar, R.; Vijayakumar, S. Adsorption of Mn Atom on Pristine and Defected Graphene: A Density Functional Theory Study. *J. Mol. Model.* **2017**, *23*, 132.

(48) Guo, Q.; Dedkov, Y.; Voloshina, E. Intercalation of Mn in Graphene/Cu(111) Interface: Insights to the Electronic and Magnetic Properties from Theory. *Sci. Rep.* **2020**, *10*, 21684.

(49) Mandale, A.; Badrinarayanan, S.; Date, S.; Sinha, A. Photoelectron-Spectroscopic

Study of Nickel, Manganese and Cobalt Selenides. *J. Electron Spectrosc. Relat. Phenom.* **1984**, *33*, 61–72.

(50) Ferrari, A. C. Raman Spectroscopy of Graphene and Graphite: Disorder, Electron–Phonon Coupling, Doping and Nonadiabatic Effects. *Solid State Commun.* **2007**, *143*, 47–57.

(51) Cun, H.; Iannuzzi, M.; Hemmi, A.; Roth, S.; Osterwalder, J.; Greber, T. Immobilizing Individual Atoms Beneath a Corrugated Single Layer of Boron Nitride. *Nano Lett.* **2013**, *13*, 2098–2103.

(52) Vita, H.; Böttcher, S.; Horn, K.; Voloshina, E.; Ovcharenko, R.; Kampen, T.; Thissen, A.; Dedkov, Y. S. Understanding the Origin of Band Gap Formation in Graphene on Metals: Graphene on Cu/Ir (111). *Sci. Rep.* **2014**, *4*, 5704.

(53) Ennos, A. The Origin of Specimen Contamination in the Electron Microscope. *Br. J. Appl. Phys.* **1953**, *4*, 101–106.

(54) Platzman, I.; Brener, R.; Haick, H.; Tannenbaum, R. Oxidation of Polycrystalline Copper Thin Films at Ambient Conditions. *J. Phys. Chem. C.* **2008**, *112*, 1101–1108.

TOC Graphic

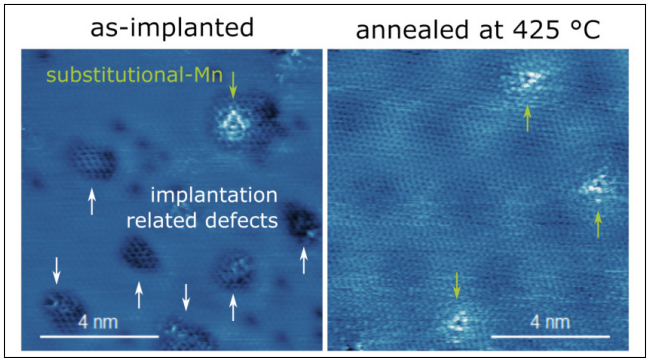
as-implanted
annealed at 425 °C
substitutional-Mn
implantation
related defects
4 nm
4 nm